International Journal of Environmental Science and Technology (2019) 16:2405–2414
https://doi.org/10.1007/s13762-017-1640-4

ORIGINAL PAPER

Improved visible photocatalytic activity of TiO_2 nanoparticles to use in submerged membrane photoreactor for organic pollutant degradation

V. Vatanpour[1] · **A. Karami**[1] · **M. Sheydaei**[1]

Received: 20 August 2017 / Revised: 9 November 2017 / Accepted: 22 December 2017 / Published online: 16 January 2018

Abstract
In this study, photocatalytic activity of TiO_2 nanoparticles under visible light was improved and the modified photocatalysts were used in a pilot-scale continuous submerged photocatalytic membrane reactor (SPMR) for decolorization of Reactive Orange 29 (RO29) under visible light irradiation. The Taguchi method was used to optimize the activation of TiO_2 nanoparticles. Effect of the activation precursors (urea, thiourea, ammonium thiocyanate and sulfanilic acid), TiO_2: precursors w/w ratio (1:1–1:6), activation time (1–7 h) and activation temperature (350–500 °C) on the visible photocatalytic efficiency of the nanoparticles was investigated to achieve maximum decolorization efficiency. X-ray diffraction, scanning electron microscopy, Fourier transform infrared and diffuse reflection spectroscopy analysis were used to characterize the photocatalysts. The results presented that the doping source and the doping source:TiO_2 ratio had the most and the lowest effect on the TiO_2 activation process, respectively. When urea was applied as an activation precursor with mass ratio of 6:1 to TiO_2 at 450 °C for 5 h, the decolorization efficiency of 84.2% was obtained in a continuous SPMR system. The RO29 degradation intermediates were analyzed by gas chromatography coupled with mass spectroscopy technique.

Keywords Environmental chemistry · Membranes · Nanotechnology · Photochemistry · Remediation · Reactor configuration

Introduction

Textile wastewater is one of the main sources of environmental contamination. They are not only colorful, but also contain great amounts of suspended organic solids (Dastkhoon et al. 2015). The physicochemical methods such as flocculation, oxidation, coagulation, membrane filtration, electrochemical techniques, adsorption, sonocatalyst and photocatalysis are usually utilized for decolorization from industrial wastewaters (Khataee et al. 2009; Madaeni et al. 2011; Zamani et al. 2014; Fakhri et al. 2016; Oskoei et al. 2016; Agarwal et al. 2017; Essandoh et al. 2017). Advanced oxidation processes (AOP), especially the photocatalysts, are the most successful processes for treatment of the dye wastewater. The key advantage of this technique is organic carbon mineralization (Oskoei et al. 2016). This process is based on the creation of highly reactive hydroxyl radicals that can degrade a wide variety of pollution (Sheydaei et al. 2014a, b). The most used photocatalyst is titanium dioxide (TiO_2). Despite the good properties of TiO_2 such as the favorable physical/chemical properties, the low cost, the availability and the stability, this photocatalyst is only active under the UV irradiation ($\lambda < 388$ nm) (Khataee et al. 2009; García-Araya et al. 2010; Royaee et al. 2011). Therefore, several attempts have been made in recent years to enhance the visible photocatalytic activity of TiO_2. Various methods have been used for this purpose such as doping with transition metals (Umebayashi et al. 2002; Rajabi et al. 2013), reduction with hydrogen (Kılıç and Zunger 2002; Palmer et al. 2002), coupling with semiconductors and dye sensitization (Pelaez et al. 2012).

The doping with nonmetal elements is one of the most effective and widely used activation methods in which nonmetals such as B, C, N, F and S are doped into TiO_2 lattices (Ohno et al. 2004; Kobayakawa et al. 2005; Di Valentin et al.

Editorial responsibility: V.K. Gupta

✉ V. Vatanpour
vahidvatanpour@khu.ac.ir; vahidvatanpoor@yahoo.com

[1] Faculty of Chemistry, Kharazmi University, Tehran 15719-14911, Iran

2007; Kitano et al. 2007). Among these nonmetals, nitrogen is considered as the most effective ones. The presence of donor energy states consists of N2p and O2p in the valance band of N–TiO_2 enhances the visible photocatalytic activity of this semiconductor (Asahi et al. 2001; Xing et al. 2009).

Furthermore, separation of TiO_2 particles from suspension is another major obstacle associated with the suspended photocatalytic systems. Immobilization of the particles on a substrate is a way to eliminate the particle recovery step (Tsumura et al. 2002; Ménesi et al. 2008). However, in this condition, the reduced catalyst area to volume ratio of the immobilized photocatalyst causes mass transfer and diffusion limitations (Butterfield et al. 1997).

The induction of the magnetic field (Beydoun et al. 2000) and pH adjustment (Fernande-Ibanez et al. 2003) are methods alternatively have been carried out to recovery of the nanoparticles from the suspended systems. In these methods, the nanoparticles are lost during the withdrawing of treated water. Applying the suitable membrane is another operative method to efficient separation of the suspended photocatalyst particles from treated water (Weimin and Geissen 2001; Vatanpour et al. 2017). In this process, photocatalytic treatment of the polluted water and filtration of treated water are done simultaneously in photocatalytic membrane reactors (PMRs) (Mozia 2010).

In recent years, the statistical experimental designs have been widely used to improve the quality of the processes by optimizing the effective parameters (Fakhri et al. 2016). The Taguchi method is a popular experimental design method, which provides maximum and reliable data using fewer possible experiments (Pourjafar et al. 2013).

Aim of this work is optimization of TiO_2 modification for visible photocatalytic degradation process in a continuous pilot-scale submerged photocatalytic membrane reactor (SPMR). Polyvinylidene fluoride (PVDF) membrane was fabricated and used to separate continuously the activated TiO_2 nanoparticles from the treated wastewater. To improve visible photocatalytic activity of TiO_2, four precursors including urea, thiourea, ammonium thiocyanate and sulfanilic acid at various mass ratios were applied at different doping times and temperatures. For determination of optimum synthesis parameters, the Taguchi method was used. The efficiency of activated TiO_2 was evaluated in the SPMR for degradation of Reactive Orange 29 (RO29) as a model pollutant under visible light irradiation. All the test results reported in this research are based on tests conducted in July to September 2016 in Karaj city in Iran.

Materials and methods

Materials

Commercial TiO_2–P25 was purchased from Degussa (Germany). PVDF (Kynar® K-761) powder was purchased from Elf Atochem (UK). *N*-methyl pyrrolidone (NMP) as a solvent of PVDF, urea, thiourea, ammonium thiocyanate and sulfanilic acid were obtained from Merck (Germany). Visible lamp (FML, 36W) was purchased from Omid Padideh Ghostar, Iran.

The Reactive Orange 29 dye, a commercial reactive azo dye, (Boyakhsaz Co., Iran) with molecular weight of 599.34 g/mol was chosen as a model pollutant, which its structure is presented in Fig. 1.

Experimental design for synthesis of visible activated TiO_2

The Taguchi method was used to design the experiments for simultaneous investigation of the effect of various operational factors and optimize TiO_2 visible photocatalytic activation. Experiments were designed according to the effective factors including TiO_2 activation precursors, mass ratio of the activation precursors to TiO_2, activation time, and activation temperature. The experiments were designed according to the L_{16} orthogonal array of the Taguchi method. Designed experimental runs and the levels of the effective factors are shown in Table 1.

On the basis of the designed conditions, first, TiO_2 nanoparticles were activated by mechanical mixing method with the activation precursors in designed weight ratios and then calcinated for dedicated time at specified temperature. The resulted powders were cooled at room temperature and washed with ethanol and deionized water several times. Finally, the products were dried at 70 °C.

PVDF membrane and SPMR

To synthesis flat sheet microfiltration PVDF membranes, non-solvent-induced phase inversion method was used (Arefi-Oskoui et al. 2016). First, the PVDF polymer was dissolved in NMP to prepare 12 wt% solution. After that, the

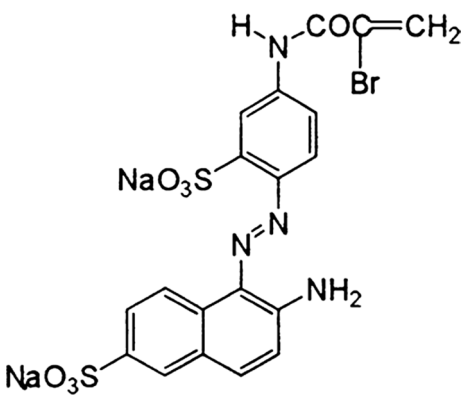

Fig. 1 Chemical structure of Reactive Orange 29

Table 1 Taguchi's L16 orthogonal design and related experimental results

Exp. Nos.	Control factors				Response
	Activation source: TiO_2 ratio	Temperature (°C)	Time (min)	Doping source	Decolorization efficiency (%)
1	1:1	350	1	Urea	63.2
2	1:1	400	3	Thiourea	71.5
3	1:1	450	5	Sulfanilic acid	63.1
4	1:1	500	7	Ammonium thiocyanate	60.3
5	2:1	350	3	Sulfanilic acid	14.0
6	2:1	400	1	Ammonium thiocyanate	80.2
7	2:1	450	7	Urea	75.7
8	2:1	500	5	Thiourea	58.9
9	4:1	350	5	Ammonium thiocyanate	64.5
10	4:1	400	7	Sulfanilic acid	33.7
11	4:1	450	1	Thiourea	68.7
12	4:1	500	3	Urea	53.3
13	6:1	350	7	Thiourea	79.9
14	6:1	400	5	Urea	82.8
15	6:1	450	3	Ammonium thiocyanate	74.3
16	6:1	500	1	Sulfanilic acid	23.8

solution was completely homogenized and heated at 50 °C to remove air bubbles. The solution was cast by a homemade applicator on a nonwoven fabric to form a film layer at a nominal thickness of 170 µm. The resulted films were immediately immersed into a coagulation bath containing distilled water at room temperature for solidification.

The SPMR setup used in this work (Fig. 2) consists of: (1) a polluted water storage tank; (2) a pump for continuous flow of polluted water into the SPMR; (3) 5.6 L stainless steel SPMR system including: a submerged membrane cell with effective membrane area of 140 cm^2, submerged visible lamp(s) to provide radiation energy required for photocatalytic process, a pH-meter electrode, a thermometer sensor, an air diffuser and a jacket with the flow of cooling water to control the temperature of the SPMR; (4) a peristaltic pump for continuous suction of the treated water from the submerged membrane cell, which cause continuous filtration and separation of treated water from the photocatalyst nanoparticles; and (5) a treated water storage tank (Vatanpour et al. 2017).

The air diffuser was used to bubble air into the solution and surface of the membrane cell to provide required dissolved oxygen for photoreaction, suspend the photocatalyst nanoparticles and prevent the fouling of the membrane surface. The membrane filtration was continuously performed using a peristaltic pump. The contents of the SPMR were mixed at 600 rpm using a magnetic stirrer.

Analytical procedures

The obtained photocatalyst nanoparticles were characterized by X-ray diffraction (XRD) analysis using Siemens X-ray diffraction D5000, with Cu $K\alpha$ radiation ($\lambda = 1.541874$ Å) in the range of 10°–80° for 2θ angle at 40 kV and 30 mA. The average size of crystallites was calculated using the Scherrer equation. The morphology of the samples was observed using scanning electron microscope (SEM, Tescan, Czech Republic). Transmission electron microscopy (TEM) image of the nanoparticles was recorded using Philips CM 10, high tension 100 kV. To record Fourier transform infrared

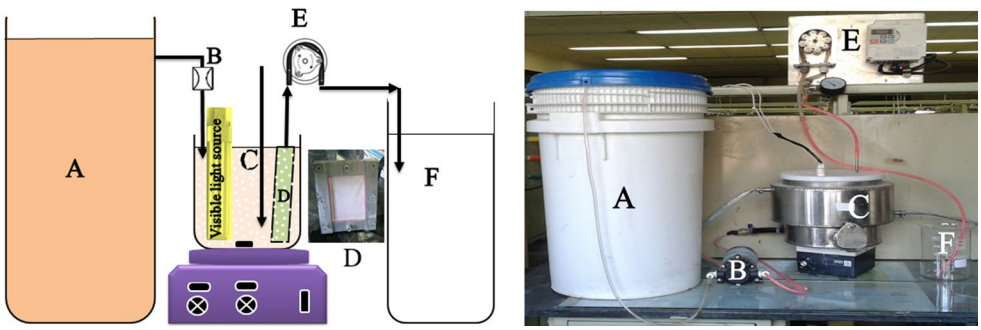

Fig. 2 Schematic and real images of SPMR setup containing (*A*) polluted water storage tank, (*B*) pump for continuous flow polluted water into the SPMR, (*C*) 5.6 L stainless steel SPMR system, (*D*) submerged membrane cell (*E*) a peristaltic pump for continuous suction of treated water from submerged membrane cell and (*F*) treated water storage tank

(FT-IR) spectra, a RIX FT-IR 2400 Perkin-Elmer spectrometer was employed using the KBr pellet technique. UV–Vis diffuse reflectance spectra (DRS) were obtained by a Cray-300 UV/Vis spectrophotometer at room temperature in the wavelength range of 300–800 nm with $BaSO_4$ as the reference for the optical characterization of the products.

Visible photocatalytic degradation

In this study, visible photocatalytic performance of the activated TiO_2 nanoparticles was investigated in degradation of RO29 dye solution. Accordingly, the activated TiO_2 nanoparticles were dispersed in dye solution in the SPMR for 15 min in the absence of any light. Then, air was pumped and simultaneously the visible light was irradiated into the reactor. During all photodegradation runs, a fresh dye solution was fed into the SPMR and treated water was continuously filtered by the PVDF membrane. At different times of sampling, the RO29 concentration in the filtered solution was determined by a UV–visible spectroscopy (double beam spectrophotometer UV-210A) at $\lambda = 475$ nm. Decolorization efficiency (%) was calculated through the following equation:

$$\text{Decolorization efficiency } (\%) = \frac{C_{\text{inlet}} - C_{\text{outlet}}}{C_{\text{inlet}}} \times 100 \quad (1)$$

where C_{inlet}, and C_{outlet} are the input and output concentrations of the RO29 from the SPMR, respectively.

Gas chromatography–mass spectrometry (GC–MS) analysis was performed to evaluate the photodegradation intermediates and propose the degradation mechanism of the pollutant. Accordingly, 100 mL of RO29 solution was treated by the photocatalytic degradation process in the presence of the activated TiO_2 nanoparticles under visible light for 10 min. Organic components of the resulted solution were extracted with 30 mL of diethyl ether three times. The obtained organic solution was held to evaporate the organic solvent. The remaining solids were dissolved in 100 µL of N,O-bis-(trimethylsilyl) acetamide, and the solution was stirred for 10 min under heating at 60 °C. GC–MS apparatus (Agilent 6890 gas chromatography and 5973 mass spectrometer, Palo Alto, Canada) was used to analysis of the resulting silylated products.

Results and discussion

Characterization of PVDF membrane

The SEM images of prepared PVDF membrane are shown in Fig. 3. Figure 3a, which shows cross-sectional image of the membrane, approves that the prepared membrane consists of two layers. The top thin and dense layer of the membrane plays the role of the separator (selective layer). The bottom layer of PVDF microporous membrane has a finger-like structure with the large cavities that plays the role of the support for the surface layer. Figure 3b shows surface SEM image of this membrane that approves the development of the uniform PVDF membrane with average pore size of 80–200 nm (analyzed by *Image J* software) (Yakavalangi et al. 2017).

To show TiO_2 rejection ability of the fabricated microporous membrane, the turbidity test was made from permeated water after TiO_2 suspension filtration (without dye). The results presented that there was no TiO_2 nanoparticle permeation and the rejection was 100%.

Optimization of TiO_2 activation

According to the experimental design presented in Table 1, 16 TiO_2 activation experiments were carried out and the ability of the prepared samples was determined in the

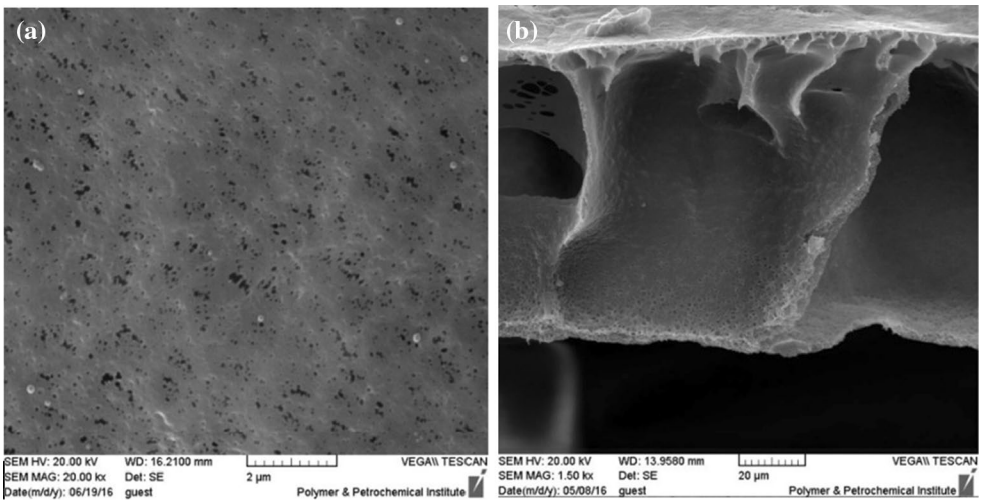

Fig. 3 SEM images of the prepared asymmetric PVDF microporous membrane

photocatalytic degradation of RO29 under visible light irradiation. The obtained results, which are shown in Table 1, were analyzed by Qualitek-4 software. Analysis of variance (ANOVA) test was conducted in order to estimate the effective parameters and their confidence levels in activation of TiO_2 nanoparticles for visible photocatalyst applications. *F*-ratio is a tool to indicate which investigated factors have a significant effect on the process. This statistic value for each factor is a ratio of the variance of factor to the variance of error. The obtained results, which are shown in Table 2, indicate that the doping source was the most effective parameter in comparison with the others.

As can be seen in Table 2, the doping source:TiO_2 ratio factor has the lowest effect on TiO_2 activation process with compared to the other factors and can be pooled to error. Table 3 shows the ANOVA results after pooling.

Predicted decolorization efficiency plots for the control factors are depicted in Fig. 4. As can be seen in Fig. 4a, all investigated ratios of the doping agent to TiO_2 had similar effect on the visible photocatalytic performance of the activated TiO_2 samples. Figure 4b shows that the increase in doping temperature up to 450 °C led to increase in decolorization efficiency. However, more increase in doping temperature caused decrease in photocatalytic decolorization efficiency. In fact, in high temperatures, the effective area of the catalyst surface reduces due to the aggregation of particles. According to the results shown in Fig. 4c, activation time of 1, 3, 5 or 7 h had relatively similar effect on the visible photocatalytic performance of the prepared

Table 2 ANOVA results

Factors	Degrees of freedom	Sum of squares	Variance	*F*-ratio
Doping source:TiO_2 ratio	3	316.418	105.472	0.722
Temperature (°C)	3	1193.128	397.709	2.913
Time (min)	3	417.397	139.132	1.019
Doping source	3	3847.870	1282.623	9.394
Other/error	3	409.578	136.526	

Table 3 ANOVA after pooling

Factors	*DF*	Sum of squares (ss)	Variance	*F*
Doping source:TiO_2 ratio	3	316.418		Pooled
Temperature (°C)	3	1193.128	397.709	3.286
Time (min)	3	417.397	139.132	1.149
Doping source	3	3847.870	1282.623	10.601
Other/error	6	725.996	120.999	

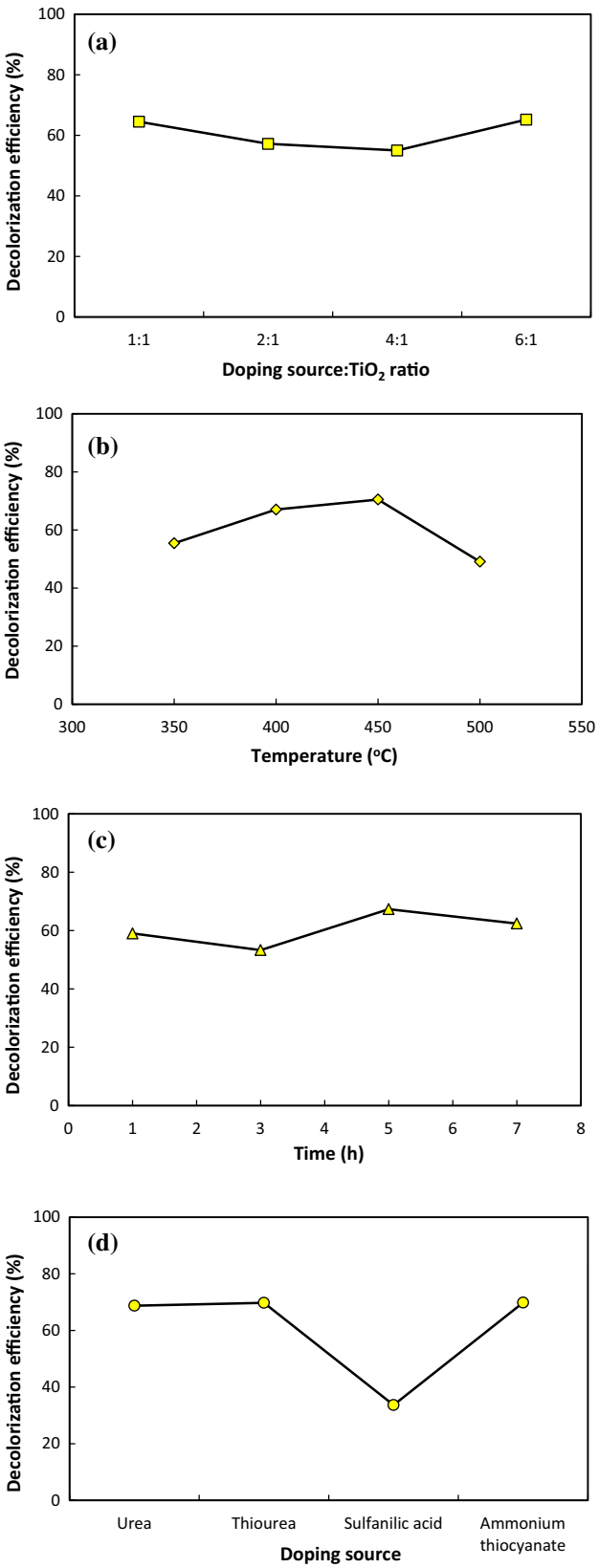

Fig. 4 Predicted main-effect plots on visible photocatalytic degradation process corresponds to Taguchi's L16 design. Effect of **a** doping source:TiO_2 ratio, **b** calcination temperature, **c** calcination time and **d** doping source

Table 4 Optimum levels of investigated factors and related RO29 degradation efficiencies

Factors	Level description	Experimentally obtained RO29 degradation (%)	Predicted RO29 degradation (%)
Doping source:TiO_2 ratio	6:1	84.2	90.2
Temperature (°C)	450		
Time (min)	5		
Doping source	Urea		

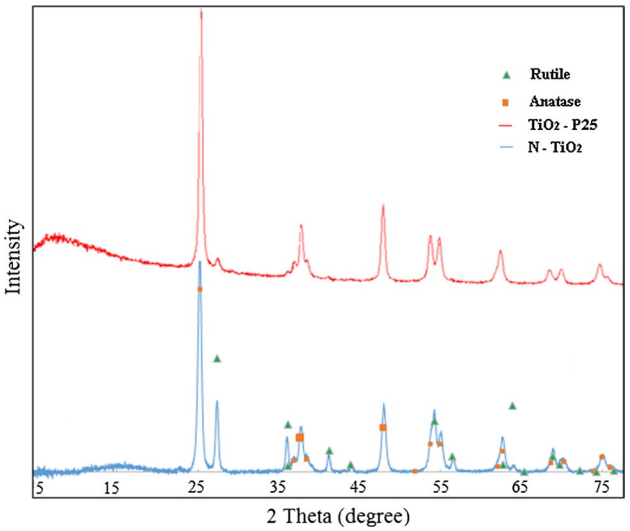

Fig. 5 XRD patterns of TiO_2–P25 and N–TiO_2 samples

catalyst. Comparison of the doping sources performance on the photocatalytic activation of TiO_2 nanoparticles under visible light indicates that except sulfanilic acid, all other doping sources show similar and considerable effect on the performance of TiO_2 doping.

Optimum values for the all investigated variables and predicted RO29 degradation value (%) at these optimum conditions are shown in Table 4. Furthermore, experimentally obtained RO29 degradation efficiency from visible photocatalytic degradation process at the optimum condition is shown in Table 4. Comparison of the predicted and experimentally obtained RO29 degradation efficiency shows that the model is applicable to estimate the best optimum conditions.

Characterization of the synthesized N-doped TiO_2

Figure 5 shows the XRD patterns of TiO_2–P25 and the activated TiO_2–P25 under the optimum conditions. The

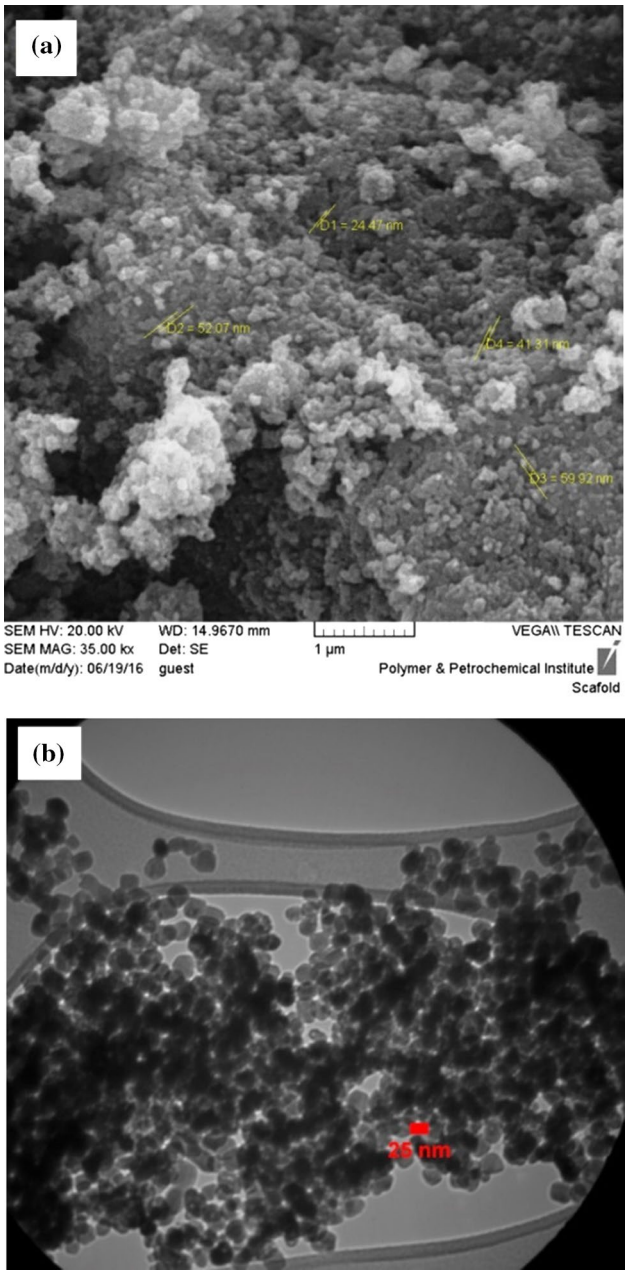

Fig. 6 **a** SEM images of N–TiO_2 and **b** TEM image of TiO_2–P25

crystalline phase of TiO_2–P25 consists of two main phases of rutile and anatase, which were characterized in Fig. 5 (Bickley et al. 1991). As can be seen, after the activation of TiO_2–P25 by nitrogen source, no significant shift of characteristic peaks was observed. This can be concluded that nitrogen source modified the surface of TiO_2 without any change in crystalline lattice of TiO_2. The crystalline size of TiO_2–P25 before and after calcination was calculated using the Debye–Scherrer equation (Patterson 1939):

$$D = K\lambda/\beta \cos\theta \quad (2)$$

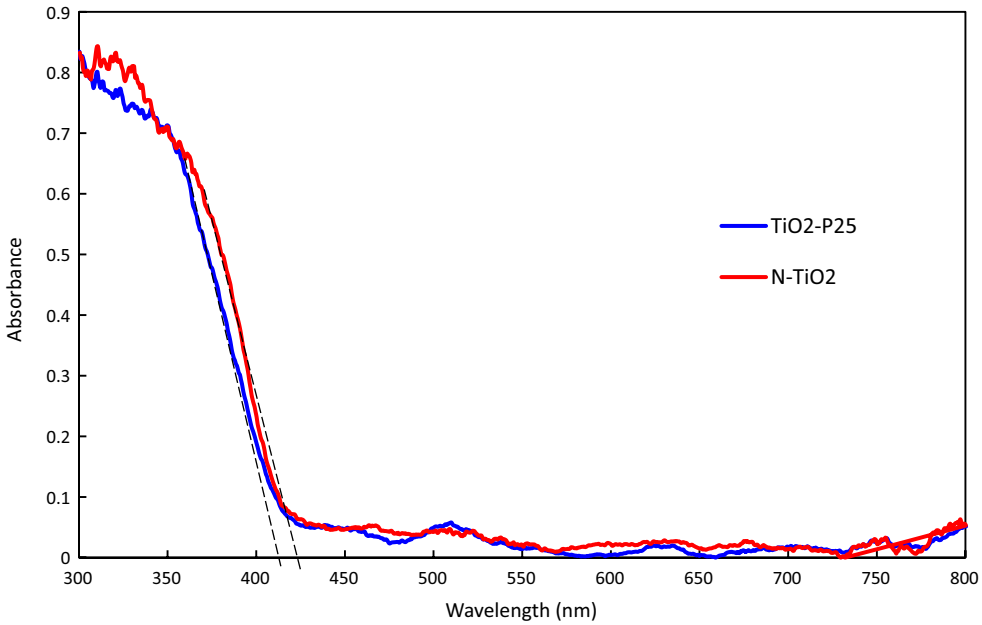

Fig. 7 UV–Vis diffuse reflectance spectra of TiO_2–P25 and N–TiO_2

where D is the average crystallite size in angstroms, K is a constant which is taken as 0.89 here, λ is the wavelength of the X-ray radiation (Cu $K\alpha = 0.15406$ nm), β is the line width at half-maximum height, and θ is the diffraction angle. It was found that the crystallite size of TiO_2–P25 slightly increased from 31.4 to 32.0 nm after calcination. This change in crystallite size has been pointed out in the studies (Porter et al. 1999; Bowering et al. 2007).

Morphological characteristics of the TiO_2–P25 and N–TiO_2 samples were characterized using SEM and TEM images. The obtained images, which are shown in Fig. 6, indicate that large quantities of N–TiO_2 particles are in nanoscale size.

Figure 7 shows the DRS of TiO_2–P25 and N–TiO_2 samples prepared at optimum conditions. Kubelka–Munk (K–M) function was used to calculate the band gap of TiO_2–P25 and N–TiO_2 according to the following equation (Eq. 3):

$$\left(\frac{hv(1-R)^2}{2R}\right)^{0.5} = C(hv - Eg) \tag{3}$$

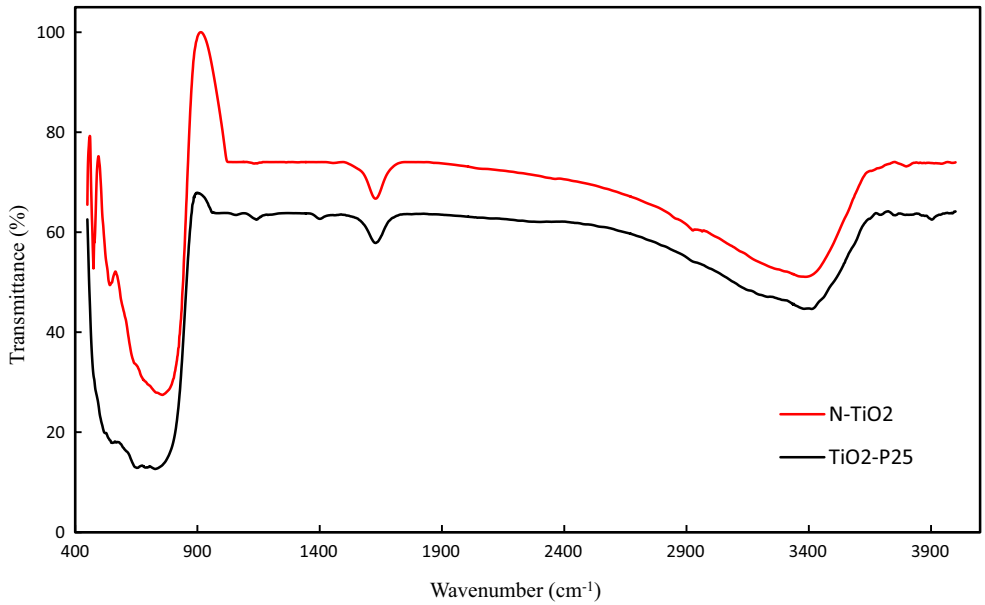

Fig. 8 FTIR spectra of TiO_2–P25 and N–TiO_2 prepared under optimum conditions

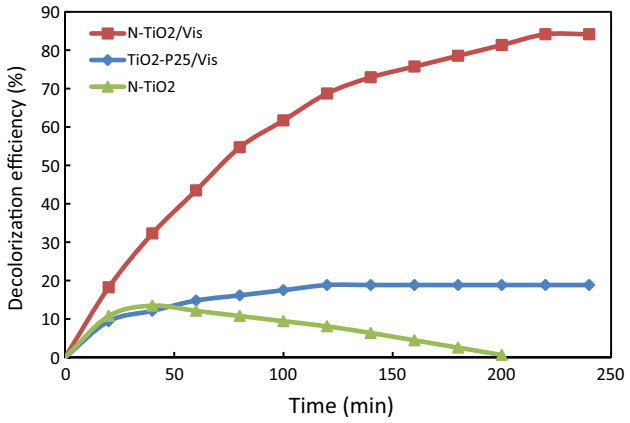

Fig. 9 Comparison of TiO_2–P25 and N–TiO_2 nanoparticles under visible light

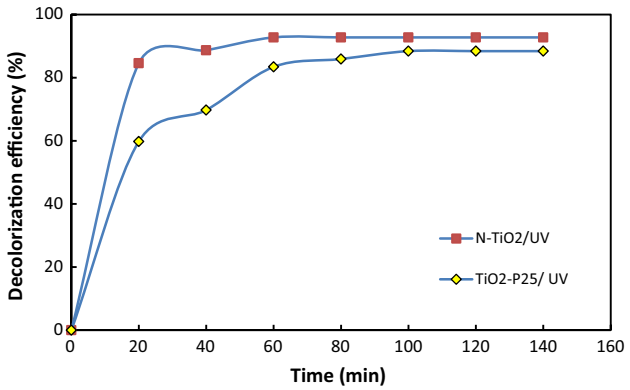

Fig. 10 Comparison of TiO_2–P25 and N–TiO_2 nanoparticles under UV light

where *R* is reflectance with respect to standard reflectance, *Eg* is band gap energy, *h* is Planck constant, *v* is frequency of light, and *C* is constant (Singh and Madras 2013). According to the obtained results, band gap energies of the TiO_2–P25 and N–TiO_2 were 2.99 and 2.88 eV, respectively. This shows that the activation of TiO_2 led to 15 nm red shift in UV–Vis absorption band of TiO_2–P25. The transition of UV–Vis spectrum to the lower energy regions is due to the narrowing in the band gap of TiO_2–P25 (Xing et al. 2009). This enables the electron transmission from the valance band to the conductive band of the activated TiO_2 sample by visible light irradiation.

Figure 8 shows the IR spectra of N–TiO_2 and TiO_2–P25 samples. The wide and strong peaks at 757 cm^{-1} can be attributed to the Ti–O (Zhou et al. 2009). A peak at 1627 cm^{-1} represents the O–H stretching tensile of molecular water adsorbed on TiO_2 (Bao et al. 2013; Cheng et al. 2013). Another peak shown at 3420 cm^{-1} corresponds to Ti–OH, which indicates the presence of hydroxyl groups in TiO_2 and O–H stretching vibration of water (Dedual et al. 2014). A sharp peak at 486 cm^{-1} of IR spectra of the N–TiO_2 can be attributed to the developing of N–Ti–N and/or N–Ti–O bonds of the activated photocatalyst (Hoseinian-Maleki et al. 2015). Development of this peak and increase of the peak intensity attributed to the hydroxyl group in N–TiO_2 compared to TiO_2–P25, which can prove that modified catalyst has higher activity than the TiO_2–P25.

Table 5 Identified by-products during degradation of RO29

No.	Compound name	Structure	Retention time (min)	Basic fragments
1	Acetic acid		1.496	117, 75, 60, 43, 45
2	*o*-Xylene		2.72	106, 91, 51
3	Cyclohexanol	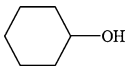	3.129	155, 129, 100, 82, 75, 58
4	Cyclohexenol	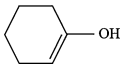	5.477	155, 127, 99, 75, 45, 27
5	Phenylmethanol	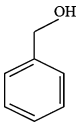	7.23	180, 165, 135, 108, 91, 79, 77
6	5-methyl-2-(1-ethylethyl)phenol	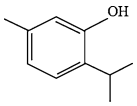	10.704	207, 96, 82, 73, 45
7	*β*-Naphthol	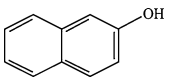	16.973	201, 144, 115, 73

Comparative studies

Visible photocatalytic degradation of 5 mg/L RO29 solution was performed using the N–TiO_2 prepared at optimum conditions to compare its ability with that of TiO_2–P25 nanoparticles in continuous process (Fig. 9). During the experiments, five 36W visible lamps were used. As can be seen in this figure, applying visible photocatalytic degradation process using TiO_2–P25 nanoparticles led to less than 20% decolorization efficiency. However, in the presence of N–TiO_2 at similar conditions, the decolorization efficiency of 84.2% was obtained, which approved the enhancement in visible photocatalytic performance of TiO_2–P25 nanoparticles through the activation process. Furthermore, the ability of N–TiO_2 nanoparticles on adsorption of RO29 in a continuous process was investigated. According to the obtained results shown in Fig. 9, the decolorization efficiency was increased and then decreased with time, due to the accumulation of the adsorption sites of N–TiO_2 nanoparticles by the adsorbed RO29 dye molecules (Sheydaei et al. 2014a,

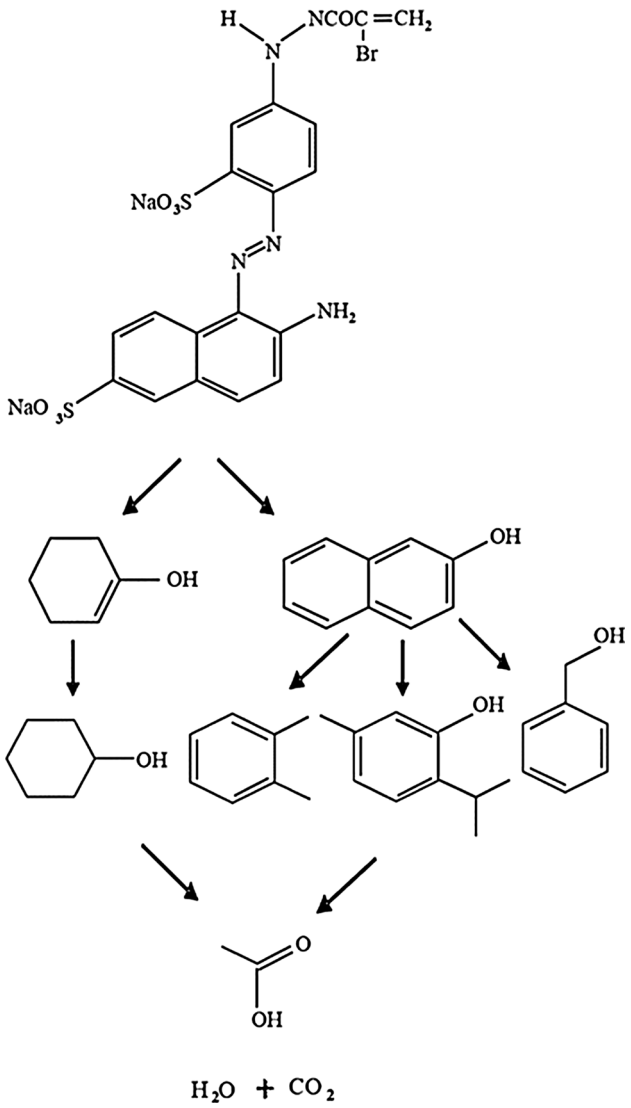

Fig. 11 Proposed RO29 degradation pathway in SMPR

b). Comparison of the results obtained from adsorption and visible photocatalytic degradation of RO29 using N–TiO_2 nanoparticles approved the considerable visible photocatalytic ability of the activated TiO_2 nanoparticles.

Effect of TiO_2 activation on photocatalytic ability of this semiconductor under UV irradiation was evaluated by comparing its ability in photocatalytic decolorization of RO29 solution with the TiO_2–P25. Figure 10 shows 88.4% decolorization in the presence of TiO_2–P25; however, this amount for N–TiO_2 was enhanced up to 92.7%. This shows that TiO_2 activation enhanced photocatalytic ability of this semiconductor under UV as well as visible irradiations.

In order to identify the degradation pathway of RO29 in the SMPR, the intermediates generated during the degradation process were analyzed by GC–MS. The analyzed constituents were identified by matching their spectra with those recorded in the MS library (Wiley 7n). Seven compounds that are listed in Table 5 were successfully detected. Furthermore, several other chromatographic peaks were also found but could not be positively identified. The product distribution results suggest that the degradation process is done by degradation of RO29 to form the β-Naphthol, Cyclohexenol, *o*-Xylene, Cyclohexanol, Cyclohexenol, phenylmethanol and 5-methyl-2-(1-ethylethyl) phenol. Oxidation of these products gives acetic acid that is converted directly into CO_2 and H_2O as can be seen in Fig. 11.

Conclusion

In this study, the photocatalytic activity of TiO_2 under the visible light was improved by nitrogen doping process. The prepared N–TiO_2 photocatalyst was optimized using the Taguchi method. Finally, the optimized sample was used in a continuous photocatalytic membrane reactor for dye degradation. According to the obtained results, urea as the nitrogen doping precursor with 6:1 ratio to TiO_2, 5 h doping time and 450 °C doping temperature were optimum conditions for enhancement of the visible photocatalytic ability of TiO_2 nanoparticles. The PVDF membrane shows good ability to separation of the nanoparticles. Using N–TiO_2 prepared at the optimum conditions, photocatalytic decolorization efficiency of 84.2% was experimentally obtained. The degradation of RO29 in the SMPR was identified using GC–MS.

Acknowledgement The authors thank the Kharazmi University, Iran, for financial and other supports.

References

Agarwal S, Tyagi I, Gupta VK, Fakhri A, Shahidi S (2017) Sonocatalytic, sonophotocatalytic and photocatalytic degradation of morphine using molybdenum trioxide and molybdenum disulfide nanoparticles photocatalyst. J Mol Liq 225:95–100

Arefi-Oskoui S, Vatanpour V, Khataee A (2016) Development of a novel high-flux PVDF-based ultrafiltration membrane by embedding Mg–Al nanolayered double hydroxide. J Ind Eng Chem 41:23–32

Asahi R, Morikawa T, Ohwaki T, Aoki K, Taga Y (2001) Visible-light photocatalysis in nitrogen-doped titanium oxides. Science 293:269–271

Bao N, Niu JJ, Li Y, Wu GL, Yu XH (2013) Low-temperature hydrothermal synthesis of N-doped TiO_2 from small-molecule amine systems and their photocatalytic activity. Environ Technol 34:2939–2949

Beydoun D, Amal R, Low GK-C, McEnvoy S (2000) Novel photocatalyst: titanium coated magnetic-activity and photodissolution. J Phys Chem B 104:4387–4396

Bickley RI, Gonzalez-Carreno T, Lees JS, Palmisano L, Tilley RJ (1991) A structural investigation of titanium dioxide photocatalysts. J Solid State Chem 92:178–190

Bowering N, Croston D, Harrison PG, Walker GS (2007) Silver modified Degussa P25 for the photocatalytic removal of nitric oxide. Int J Photoenergy 2007:1–8

Butterfield M, Christensen PA, Curtis TP, Gunlazaurd J (1997) Water disinfection using an immobilized titanium dioxide film in a photochemical reactor with electric field enhancement. Water Res 31:675–677

Cheng X, Yu X, Xing Z (2013) Enhanced photoelectric property and visible activity of nitrogen doped TiO_2 synthesized from different nitrogen dopants. Appl Surf Sci 268:204–208

Dastkhoon M, Ghaedi M, Asfaram A, Goudarzi A, Langroodi SM, Tyagi I, Agarwal S, Gupta VK (2015) Ultrasound assisted adsorption of malachite green dye onto ZnS: Cu–NP–AC: Equilibrium isotherms and kinetic studies—response surface optimization. Sep Purif Technol 156:780–788

Dedual G, MacDonald MJ, Alshareef A, Wu Z, Tsang DC, Yip AC (2014) Requirements for effective photocatalytic oxidative desulfurization of a thiophene-containing solution using TiO_2. J Environ Chem Eng 2:1947–1955

Di Valentin C, Finazzi E, Pacchioni G, Selloni A, Livraghi S, Paganini MC, Giamello E (2007) N-doped TiO_2: theory and experiment. Chem Phys 339:44–56

Essandoh M, Wolgemuth D, Charles UPJ, Mohan D, Mlsna T (2017) Phenoxy herbicide removal from aqueous solutions using fast pyrolysis switchgrass biochar. Chemosphere 174:49–57

Fakhri A, Rashidi S, Tyagi I, Agarwal S, Gupta VK (2016) Photodegradation of Erythromycin antibiotic by γ–Fe_2O_3/SiO_2 nanocomposite: response surface methodology modeling and optimization. J Mol Liq 214:378–383

Fernande-Ibanez P, Blanco J, Malato S, Nieves FJ (2003) Application of the colloidal stability of TiO_2 particles for recovery and reuse in solar photocatalysis. Water Res 37:3180–3188

García-Araya JF, Beltran FJ, Aguinaco A (2010) Diclofenac removal from water by ozone and photolytic TiO_2 catalysed processes. J Chem Technol Biotechnol 85:798–804

Hoseinian-Maleki F, Nemati A, Joya YF (2015) Synthesis of C–N–Y tri-doped TiO2 photo-catalyst for MO degradation and characterization. Mater Res Express 2:1–12

Khataee AR, Vatanpour V, Amani Ghadim AR (2009) Decolorization of C.I. Acid blue 9 solution by UV/Nano-TiO_2, Fenton, Fenton-like, electro-Fenton and electrocoagulation processes: a comparative study. J Hazard Mater 161:1225–1233

Kılıç Ç, Zunger A (2002) N-type doping of oxides by hydrogen. Appl Phys Lett 81:73–75

Kitano M, Matsuoka M, Ueshima M, Anpo M (2007) Recent developments in titanium oxide-based photocatalysts. Appl Catal A Gen 325:1–14

Kobayakawa K, Murakami Y, Sato Y (2005) Visible-light active N-doped TiO_2 prepared by heating of titanium hydroxide and urea. J Photochem Photobiol, A 170:177–179

Madaeni SS, Vatanpour V, Monfared HA, Shamsabadi AA, Majdian K, Laki S (2011) Removal of coke particles from oil contaminated marun petrochemical wastewater using PVDF microfiltration membrane. Ind Eng Chem Res 50:11712–11719

Ménesi J, Körösi L, Bazsó É, Zöllmer V, Richardt A, Dékány I (2008) Photocatalytic oxidation of organic pollutants on titania–clay composites. Chemosphere 70:538–542

Mozia S (2010) Photocatalytic membrane reactors (PMRs) in water and wastewater treatment. A review. Sep Purif Technol 73:71–91

Ohno T, Akiyoshi M, Umebayashi T, Asai K, Mitsui T, Matsumura M (2004) Preparation of S-doped TiO_2 photocatalysts and their photocatalytic activities under visible light. Appl Catal A Gen 265:115–121

Oskoei V, Dehghani MH, Nazmara S, Heibati B, Asif M, Tyagi I, Agarwal S, Gupta VK (2016) Removal of humic acid from aqueous solution using UV/ZnO nano-photocatalysis and adsorption. J Mol Liq 213:374–380

Palmer RA, Doan TM, Lloyd PG, Jarvis BL, Ahmed NU (2002) Reduction of TiO_2 with hydrogen plasma. Plasma Chem Plasma Process 22:335–350

Patterson AL (1939) The Scherrer formula for X-ray particle size determination. Phys Rev 56:978–982

Pelaez M, Nolan NT, Pillai SC, Seery MK, Falaras P, Kontos AG, Dunlop PSM, Hamilton JWJ, Byrne JA, O'Shea K, Entezari MH, Dionysiou DD (2012) A review on the visible light active titanium dioxide photocatalysts for environmental applications. Appl Catal B Environ 125:331–349

Porter JF, Li YG, Chan CK (1999) The effect of calcination on the microstructural characteristics and photoreactivity of Degussa P-25 TiO_2. J Mater Sci 34:1523–1531

Pourjafar S, Jahanshahi M, Rahimpour A (2013) Optimization of TiO_2 modified poly(vinyl alcohol) thin film composite nanofiltration membranes using Taguchi method. Desalination 315:107–114

Rajabi HR, Khani O, Shamsipur M, Vatanpour V (2013) High-performance pure and Fe^{3+}-ion doped ZnS quantum dots as green nanophotocatalysts for the removal of malachite green under UV-light irradiation. J Hazard Mater 250–251:370–378

Royaee SJ, Sohrabi M, Soleymani F (2011) Performance of a photo-impinging streams reactor for the phenol degradation process. J Chem Technol Biotechnol 86:205–212

Sheydaei M, Aber S, Khataee A (2014a) Degradation of amoxicillin in aqueous solution using nanolepidocrocite chips/H_2O_2/UV: optimization and kinetics studies. J Ind Eng Chem 20:1772–1778

Sheydaei M, Aber S, Khataee A (2014b) Preparation of a novel γ-FeOOH-GAC nano composite for decolorization of textile wastewater by photo Fenton-like process in a continuous reactor. J Mol Catal A: Chem 392:229–234

Singh SA, Madras G (2013) Photocatalytic degradation with combustion synthesized WO_3 and WO_3TiO_2 mixed oxides under UV and visible light. Sep Purif Technol 105:79–89

Tsumura T, Kojitani N, Umemura H, Toyoda M, Inagaki M (2002) Composites between photoactive anatase-type TiO_2 and adsorptive carbon. Appl Surf Sci 196:429–436

Umebayashi T, Yamaki T, Itoh H, Asai K (2002) Analysis of electronic structures of 3d transition metal-doped TiO_2 based on band calculations. J Phys Chem Solids 63:1909–1920

Vatanpour V, Karami A, Sheydaei M (2017) Central composite design optimization of Rhodamine B degradation using TiO_2 nanoparticles/UV/PVDF process in continuous submerged membrane photoreactor. Chem Eng Process Process Intensif 116:68–75

Weimin XI, Geissen SU (2001) Separation of titanium dioxide from photocatalytically treated water by cross-flow microfiltration. Water Res 35:1256–1262

Xing M, Zhang J, Chen F (2009) New approaches to prepare nitrogen-doped TiO_2 photocatalysts and study on their photocatalytic activities in visible light. Appl Catal B Environ 89:563–569

Yakavalangi ME, Rimaz S, Vatanpour V (2017) Effect of surface properties of polysulfone support on the performance of thin film composite polyamide reverse osmosis membranes. J Appl Polym Sci 134:44444

Zamani N, Rajabi HR, Taghdiri M, Fakhaei AS, Vatanpour V (2014) Comparative study of different systems for adsorption and catalytic oxidation of hexamine in industrial wastewaters. J Ind Eng Chem 20:37–45

Zhou L, Deng J, Zhao Y, Liu W, An L, Chen F (2009) Preparation and characterization of N–I co-doped nanocrystal anatase TiO_2 with enhanced photocatalytic activity under visible-light irradiation. Mater Chem Phys 117:522–527